Characterisation of the diffusion properties of metal foam hybrid flow-fields for fuel cells using optical flow visualisation and X-ray computed tomography

A. Fly[a], D. Butcher[a], Q. Meyer[b,d], M. Whiteley[b], A. Spencer[a], C. Kim[c], P.R. Shearing[b], D.J.L. Brett[b], R. Chen[a,*]

[a] Department of Aeronautical and Automotive Engineering, Loughborough University, UK
[b] Electrochemical Innovation Lab, Department of Chemical Engineering, University College London, UK
[c] Korea Institute of Energy Research, South Korea
[d] Nanoelectrochemistry Group, School of Chemistry, UNSW, Sydney 2052, Australia

HIGHLIGHTS

- Optical analysis of flow distribution in porous metal foam flow fields.
- Findings show Increasing manifold inlet area reduces residence time and pressure drop.
- New hybrid foam using pressed channels demonstrates controllable fluid distribution.
- Hybrid foam performance correlated to X-ray CT scans and porosity analysis.

ARTICLE INFO

ABSTRACT

The flow distribution behaviour of open-cell metallic foam fuel cell flow-fields are evaluated using ex-situ optical analysis and X-ray computed tomography (X-ray CT). Five different manifold designs are evaluated and flow distribution and pressure drop quantitatively evaluated with reference to applications in polymer exchange membrane fuel cells (PEMFC) and heat exchangers.

A 'hybrid' foam flow-field is presented consisting of flow channels pressed into the foam to promote flow distribution and reduce pressure drop. Cross- and through-channel pressure drop measurements are conducted, along with X-ray CT analysis.

Results using dyed water show that metallic foams provide excellent fluid distribution across the fuel cell flow-field, closely following the theoretical filling rate. The time for dye to cover 80% of the flow-field area was 61% faster with a foam flow-field then with no flow-field present. Pressure drop was seen to reduce with increasing foam inlet area to levels comparable to multi-serpentine flow-fields. The introduction of flow channels in the foam can further reduce pressure drop and provide more even filling of the foam, at the expense of increased residence time.

1. Introduction

Porous metallic foams are a class of material that have seen increasing research interest in recent years, with broad applications ranging from acoustic absorption and vibration control to fuel cells and catalyst carriers [1]. Metallic foams possess a beneficial combination of properties, namely high porosities, low densities and large specific surface areas, whilst maintaining high electrical and thermal conductivities. Metallic foams are separated into two groups; closed-cell (where the internal surfaces are not accessible), and open-cell (where the internal surfaces can be accessed by a working fluid) [2]. The behaviour of the working fluid in contact with open-cell metallic foams is an area of research which has been explored for several different energy applications, most notably polymer exchange membrane fuel cells (PEMFCs).

Large surface area-to-volume ratios, high thermal conductivity and high permeability, make open-cell metallic foams ideal materials for effective heat transfer. One of the first to investigate this was Boomsma

---

et al. [3], who demonstrated thermal resistances two to three times lower for compressed aluminium foam compared to conventional heat exchangers for the same pumping power when using a liquid coolant. Huisseune et al. [4] replaced the air side of a fin and tube heat exchanger with metallic foam in numerical simulations, showing improved heat transfer to fan power ratio compared to louvered fins, but over a larger frontal area. Other works have considered the influence of fouling [5], surface roughness [6] and use in improving the thermal conductivity of phase-change materials [7].

Open-cell metallic foams have been used as cooling plates in hydrogen fuel cell stacks as a replacement for conventional machined or pressed flow channels. Odabaee et al. [8] conducted experimental studies on replacing liquid cooling in parallel channels with air cooling in aluminium foam. Afshari et al. [9] conducted numerical simulations comparing different fuel cell cooling channels to metallic foams.

In addition to being used for coolant, open-cell metallic foams have seen successful deployment as a replacement for conventional land and channel reactant flow distributors in fuel cells [10] [11]. In this application, the metallic foam serves multiple purposes of distributing reactants, removing product water, conducting electricity, conducting heat and providing mechanical integrity. The use of metallic foam flow-fields in PEMFCs was first demonstrated by Murphy et al. [12] in an eight-cell stack with nickel foam flow-fields. Kumar and Reddy [13] [14] [15], then compared the performance of conventional multi-parallel land and channel flow channels to a Ni-Cr foam, showing improved performance of the foam, particularly at high current densities where mass transport phenomena dominate.

More recently, other studies have investigated the use of metallic foams on PEMFCs [16] [17] [18], direct methanol fuel cells (DMFC) [19] [20], alkaline fuel cells (AFC) [21] and high temperature polymer exchange membrane fuel cells (HTPEMFC) [22]. However, only a few studies have evaluated the fluid behaviour inside the flow-fields. Tsai et al. [23] conducted experimental comparisons of four different foam flow-fields in a PEMFC by putting physical separators into the flow-fields to control flow direction; showing that three parallel sections within the foam gave best pressure drop to electrochemical performance compromise. Kariya et al. [24] conducted a similar study using sintered metal powders with different flow-field partitions. Tabe et al. [25] conducted an in-situ optical study of a metallic foam flow-field in a PEMFC, correlating current density to liquid water accumulation and temperature distribution, demonstrating improved stability when using a hydrophilic foam treatment. Murphy et al. [12] used dyed water to visualise flow distribution in an expanded titanium porous flow-field by matching fluid Reynold's number to air, demonstrating good flow distribution across the cell surface after 7.0 s.

X-ray CT techniques have been used to great effect as a non-destructive means of capturing and analysing the internal three-dimensional (3D) structure of materials. In the fuel cell literature, X-ray CT scanning and 3D reconstruction techniques have been used for porosity-tortuosity analysis of membrane electrode assembly (MEA) structures [26] [27] and to generate fibre-level geometries of gas diffusion layers for two-phase Lattice-Boltzmann simulations [28] [29].

To date, there is yet to be an experimental evaluation of macroscopic flow distribution in metallic foam fuel cell flow-field designs. In this work, the flow distribution of five different metallic foam manifold designs are quantitatively evaluated through flow visualisation of dyed liquid water at Reynolds numbers representative of air flow rates in PEMFCs. A new hybrid foam flow-field is introduced, consisting of pressed channels in the metallic foam; porosity distribution of the new channel is assessed using X-ray computed tomography and experimental pressure drop measurements. The influence of three different hybrid flow channel geometries on flow distribution are then assessed. This work will help to inform future fuel cell flow-field designs.

Table 1
Metal foam parameters.

Parameter	Value	Source
Thickness	1.6 mm	Manufacturer
Cell size	110 ppi	Manufacturer
Density	262.5 kg/m^3	Manufacturer
Overall porosity	86.5%	X-ray CT
Flow porosity	84.0%	X-ray CT

2. Experimental

Three separate experimental procedures are used to characterise and understand the flow behaviour of the metallic foam; X-ray computed tomography (X-ray CT), pressure drop measurements and optical flow analysis. The same foam type is used in all tests, an open-cell nickel foam, supplied by Corun New Energy (China) in 1.6 mm thick sheets. Specification of the foam is shown in Table 1, where data is either sourced from the supplier or X-ray CT.

To promote the fluid distribution and reduce pressure drop, a hybrid porous flow channel has been developed which consists of semi-circular channels pressed into the foam to achieve regions of dense foam and regions of free space. The flow channels were manufactured by pressing 3 mm diameter stainless steel rods into the foam using a hydraulic press under a load of 3 kN. These values were chosen to give cross-sectional areas similar to flow channels in conventional PEMFCs.

2.1. X-ray CT

X-ray computed tomography images of the foam were captured using a Nikon XT 225 X-ray machine. The geometric configuration of the radiographic scans resulted in a pixel resolution of 10.8 μm, for a sample size of 1 cm × 1 cm. In all cases, an accelerating voltage of 95 kV and a current of 100 A was used to generate 3176 individual projections of the cells, with an exposure time of 1 s.

The single-phase material segmentation was reconstructed using Avizo software. The localised porosity in the z-direction (parallel-to-flow channel) was calculated from Equation (1) using ImageJ and Avizo software packages.

$$p(i, j) = 1 - \frac{1}{K} \sum_{k=1}^{K} x(i, j, k) \tag{1}$$

With p the localised porosity, (i, j) the location of a pixel over the x and y direction, k the location of the slice over the z axis, K the number of slices over the z axis ($K = 750$), and $x(i, j, k)$ the binarized value of the corresponding pixel (i, j, k). Despite the metal foam being open-cell, the foam ligaments are hollow, creating small gas voids which are inaccessible to flow. To assure the accuracy of the porosity calculations, these hollow void areas were manually filled-in before the 3D reconstruction and analysis was undertaken. In Table 1, overall porosity refers to the porosity calculated including ligament voids and flow porosity refers to the porosity calculated with the voids filled. Flow porosity is used for the remainder of this study. Scanning electron microscope (SEM) images were captured using a Hitachi TM3030 and a 15 kV accelerating voltage. The influence of the flow channel on fluid flow is discussed in Section 3.

2.2. Pressure drop testing

2.2.1. Manifold testing

A series of tests were performed to evaluate the pressure drop of different manifold and flow-field designs. Tests were conducted on a 100 × 100 × 1.6 mm foam sample pressed between 6 mm thick Perspex sheets, sealed using a 1.5 mm silicon gasket into which the flow manifolds were cut. The fixture was secured with 16 bolts tightened to
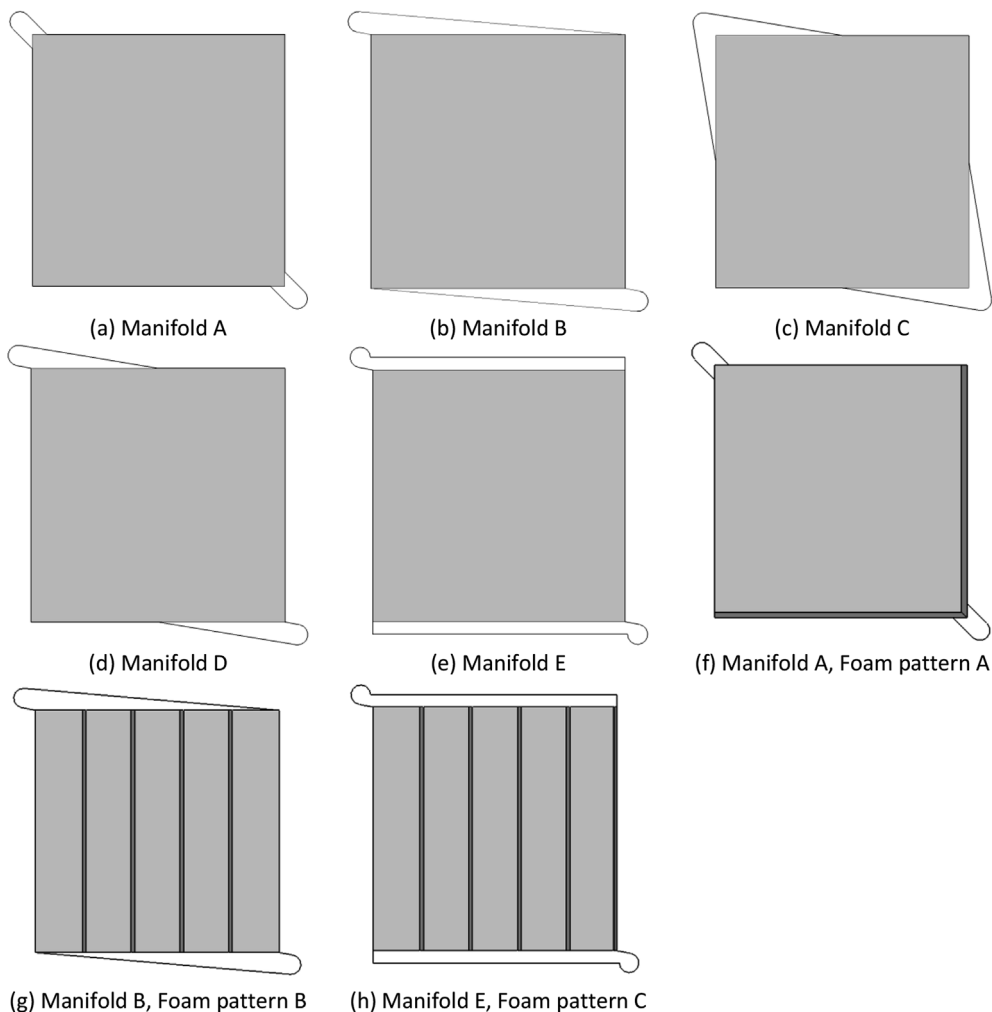
Fig. 1. Flow manifold and hybrid flow-field designs (dark grey indicates pressed channel).

3 Nm. Air was used as the working fluid, controlled by a Teledyne HFC-202 (± 0.08 lpm) mass flow controller. Pressure was measured using an RS Pro 100 mbar pressure sensor (± 0.25 mbar). Air flow rate was increased from 1 lpm to 8 lpm in 1 lpm steps. The specimen was allowed 30 s to stabilise then the pressure reading averaged over a 30 s period to minimise fluctuations. All measurements were made using a National Instruments compactDAQ data logger. Five different manifold designs and three different 'hybrid' flow-field patterns were tested. Fig. 1 shows the flow manifolds and 'hybrid' flow-field patterns; in all cases, the flow enters in the bottom right corner and exits from the top left corner.

2.2.2. 'Hybrid flow channel'

Separate pressure drop tests were conducted to evaluate the pressure drop of the foam flow channel geometry. The test fixture consists of a $55 \times 15 \times 1.6$ mm foam sample, sealed using a 1.5 mm gasket pressed between two 22 mm thick aluminium plates. The fixture is secured with eight bolts tightened to 3 Nm. The same method as described in Section 2.2.1 is used to obtain measurements, with flow direction along the 55 mm sample length. Three separate flow channels were tested, a single flow channel parallel to the flow, a single flow channel perpendicular to the flow and three flow channels perpendicular to the flow.

2.3. Flow visualisation

A water analogy of the foam is used with a back-lit dye step-in

technique to allow measurements of the flow distribution through each of the foam and manifold designs. Water can be used as a replacement fluid for air by equating the non-dimensionalised Reynolds numbers (Re) of both fluids, commonly referred to as Reynolds similarity [30]. Since the dimensional constant (d) remains unchanged, the ratio of kinematic viscosity (ν) must equal the ratio of velocity (V), shown in Equation (3) [30]. Reynolds similarity was performed for air (subscript a) at 75 °C and water (subscript w) at 20 °C using data from Ref. [31], this gives an air-to-water velocity ratio of 20.56:1.

$$Re = \frac{V_w d_w}{\nu_w} = \frac{V_a d_a}{\nu_a} \qquad (2)$$

$$\frac{V_a}{V_w} = \frac{\nu_a}{\nu_w} \qquad (3)$$

As well as reducing the required velocity, water also simplifies the visualisation procedure, allowing dye to be used and gravity as the fluid driving force. Reynolds similarity assumes surface tension and compressibility effects are negligible; these assumptions are valid in this single-phase experiment since the foam is fully immersed in the working fluid and flow is laminar ($Re_{max} = 1150$). All data presented in this work has been captured at 250 Hz, which is equivalent to 5.14 kHz in an airflow experiment at the same Reynolds number in air. Due to the backlit technique, flow is averaged over the thickness of the foam.

2.3.1. Experimental set-up and calibration

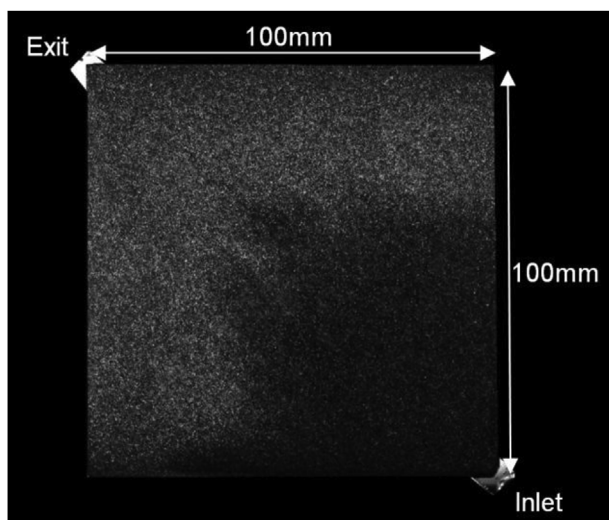For the visualisation experiments, each foam sample

Fig. 2. Example raw image (with dimensions annotated).

$(100 \times 100 \times 1.6\,\mathrm{mm})$ is pressed between transparent 6 mm Perspex sheets, and assembled as per Section 2.2.1. Flow is gravity fed to the working section from one of two header tanks; one containing a blue dye of concentration 286:1 and one containing water, selected via a valve allowing the step-in of dye. Working fluid is added from the bottom of the sample to allow air removal during initial filling. The flow rate is controlled using a needle valve and monitored via direct collection of the fluid at the outlet. The working section is backlit with red light - providing maximum absorption by the blue dye - set to achieve a suitable luminosity when observed through the metal foam as shown in Fig. 2. A monochrome Photron Fastcam Mini AX200 is used to capture images at 250 Hz, full resolution: $1024 \times 1024 – 880 \times 880$ usable to represent the working section - with an exposure time of 1 ms.

Calibration tests were carried out for each foam and manifold combination over a range of four concentrations (No dye, 2000:1, 667:1 400:1 and 286:1). It was necessary to calibrate intensity and concentration at each spatial location throughout the working section to eliminate any non-uniformity in the illumination or optical path and any non-linear effects of the signal [32], [33]. Three flow rates were tested, 56.2, 112.4 and 225.0 ml min^{-1} to give Reynolds similarity to air flow at 0.25, 0.5 and 1 A cm^{-2} current density, 2.5 stoichiometry for a 100 cm^2 active area in a PEMFC application. These values correspond to the activation, ohmic and mass transport regions of PEMFC operation [34].

2.3.2. Data processing

All images were captured using Photron PFV 3.4 software and kept

in uncompressed 8-bit format. Image and subsequent data processing and analysis were carried out using an in-house developed MATLAB® program.

As can be seen in Fig. 2, by backlighting the porous foam, there is a non-uniform penetration of light within both the areas containing dye and those without due to light reflection within the foam geometry. To alleviate this problem, the 880×880 pixel images are binned in size 10×10 pixels; leading to a physical spatial resolution of 1.13 mm^2. During the calibration procedure, the luminosity at each bin location is recorded for each of the specified dye concentrations. This produces a local calibration curve at each spatial location, to allow conversion between luminosity and concentration; scaled between 0% (no dye) and 100% (fully saturated).

For each test condition, the luminosity signals are recorded and first converted to concentration using the local calibration. To normalise the start point of each test $t = 0$ is set once 2.5% of the pixels show dye saturation – this was found to best represent when dye first enters the foam. Applying this technique results in a time history for each spatial bin location allowing the residence time to be calculated; defined as the time until each bin reaches 50% saturation. All further analysis is based on these times.

3. Results and discussion

3.1. Manifold design

3.1.1. Flow distribution

Time histories of the flow-field area coverage are shown in Fig. 3(a) at the high flow rate (225 ml min^{-1}) for the different manifolds after data processing. As described in Section 2.3.2, the area coverage is determined as the fraction of pixel bins (10×10 pixels) in the flow-field to have exceeded a dye concentration of 50%. The theoretical filling rate is calculated as the minimum time taken to fill the available fluid volume, excluding the volume occupied by the foam, at the tested flow rate. This linear relationship represents the best-case scenario.

All five manifold designs exhibit good flow distribution when combined with the metal foam flow-field, closely following the theoretical filling rate until approximately 75% of the flow-field is filled. After this point, Manifolds B and E exhibit the best flow-field coverage, reaching 95% within 4.6 s (220 ms equivalent for air). Videos of the different manifolds can be seen in the supplementary materials. Data collection for manifold C stops at 6.9 s due to filling of the camera memory buffer during this test, at this point 95% of the flow field was covered.

The influence of the metal foam on flow distribution can be clearly seen by comparing the flow-field residence times of Manifold A with and without the foam flow-field in Fig. 3(a). In the no foam case, the dye quickly travels from the inlet to exit without reaching the corners of
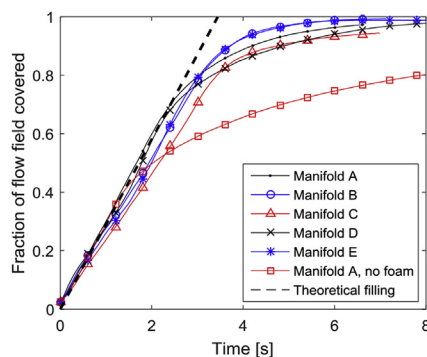
(a) area coverage of different manifold designs, 225 ml min^{-1}
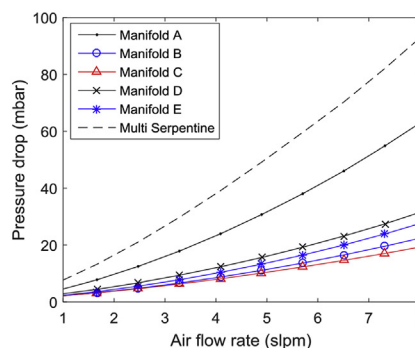
(b) pressure drop comparison of different manifolds

Fig. 3. Area coverage and pressure drop of different foam manifold designs.

(a) Manifold A

(b) Manifold B

(c) Manifold C

(d) Manifold D

(e) Manifold E

(f) Manifold A no foam

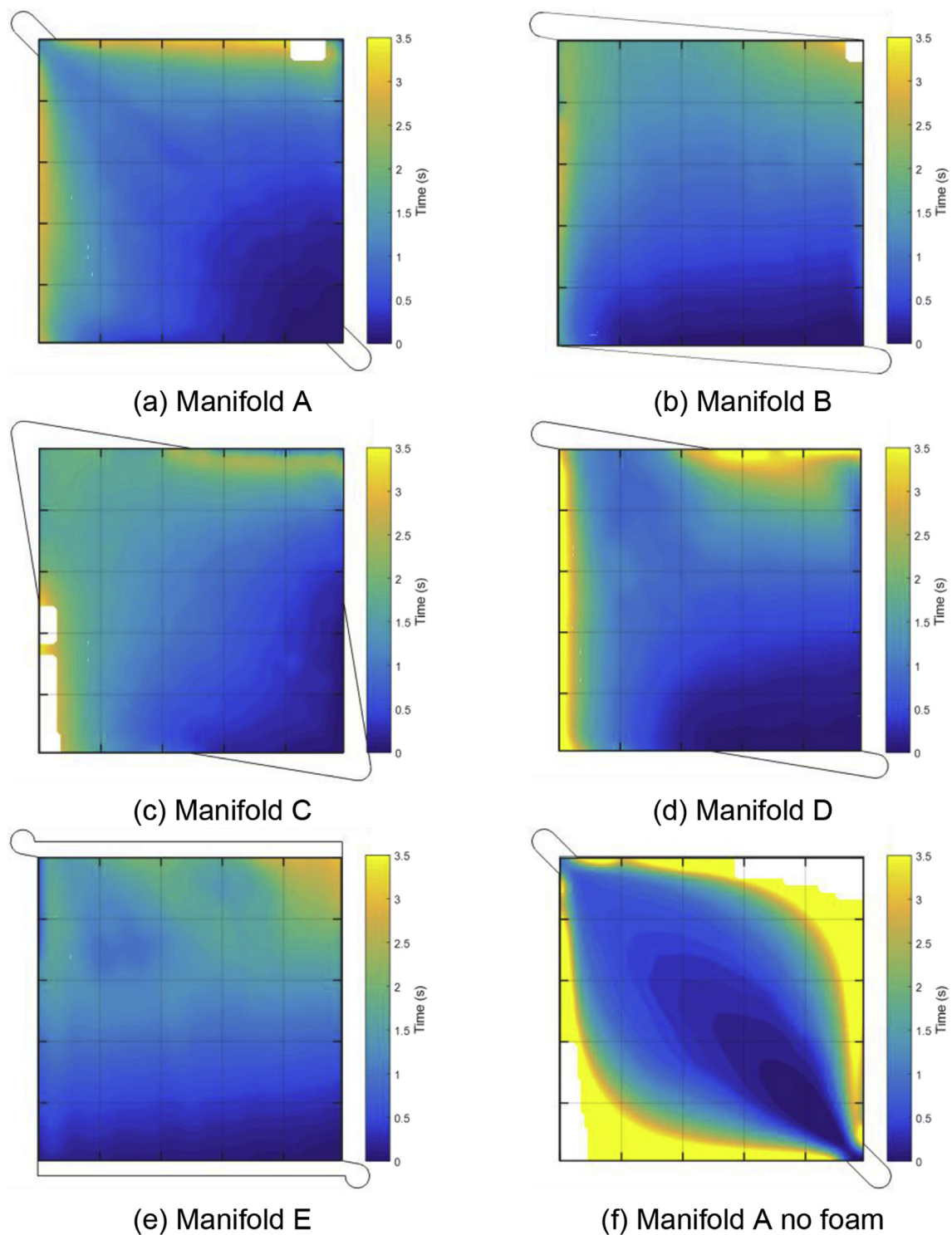**Fig. 4.** Mean residence time front for different manifold designs at 225 ml min^{-1} liquid flow rate.

the flow-field. The foam enhances flow distribution through establishing a velocity component perpendicular to the normal flow direction when the fluid contacts the foam. This cell-level flow behaviour was studied by Onstad et al. [35] using magnetic resonance velocimetry on scaled foam geometry. The authors observed perpendicular velocity components of 20–30% of the superficial velocity.

Fig. 4 maps the time taken for each pixel bin in the different manifolds to reach 50% concentration, allowing areas of fast and slow dye distribution to be identified. Manifold E shows the best flow distribution, with dye reaching over 50% of the flow-field within 2 s, the

top right corner taking up to 3 s (equivalent to 146 ms for air). Manifolds A, C and D all exhibit increased times to saturate the bottom left and top right corners. This can potentially lead to fuel starvation in fuel cells. Fig. 4(f) shows the no foam case, demonstrating increased inlet to outlet through flow behaviour. Flow-field coverage exceeding 9 s was not recorded due to the memory limitations of the camera.

Flow distribution tests were conducted at three flow rates (56.2112.4 and 225.0 ml min^{-1}) for each manifold. The time taken for 80% of the flow-field area to reach 50% dye concentration for each manifold design is shown in Table 2. This represents the point at which

Table 2
Time for 80% of the flow-field area to reach at least 50% concentration.

Manifold	225 ml min^{-1}	112.4 ml min^{-1}	56.2 ml min^{-1}
A	3.03 s	6.05 s	12.87 s
B	3.10 s	6.93 s	15.53 s
C	3.43 s	7.97 s	13.98 s
D	3.33 s	7.33 s	14.01 s
E	3.05 s	5.90 s	12.60 s
A (No foam)	7.88 s	9.24 s	13.94 s
Theoretical filling	2.76 s	5.51 s	11.03 s

only minor areas of the flow field remain without dye, as shown by the gradient change in the flow-field coverage curves of Fig. 3. The distribution times of the different manifolds with the metal foam nearly double as the flow rate is reduced by a factor of two. In comparison, the relative performance of the no foam case improves with a reduction in flow rate, indicating that diffusion plays a more predominant role in distributing fluid at lower flow rates.

3.1.2. Pressure drop

The pressure drop across fuel cell flow-fields should be minimised to reduce parasitic pumping losses and increase system efficiency. Fig. 3(b) shows the experimental pressure drop of the five different manifold designs containing metal foam at different air flow rates. For comparison, the pressure drop for 100 cm^2 active area PEMFC (Pragma Industries) using a multi-serpentine flow-field is shown. The serpentine channels have a depth of 1 mm (compared to the 1.5 mm thick foam) and was tested in-situ with a membrane electrolyte assembly. For the geometry tested 4.62 lpm is equivalent to PEMFC operation of 1 A cm^{-2} at 2.5 cathode stoichiometry.

In all cases, the pressure drop is within the same range as the multi serpentine flow field, yet systematically lower (1.6 times for Manifold A, 3.0–4.6 times for the other manifolds, with the lowest drop seen for C), highlighting the benefits of using metal foams. The reduction in pressure drop corresponds to an increase in the cross-sectional area the fluid can enter or exit the flow-field. A smaller inlet area, such as in Manifold A (17 mm^2), leads to an increased inlet velocity and higher pressure drop. Both Manifold E and C have the same inlet and exit cross-sectional areas (135 mm^2), yet C exhibits a marginally lower pressure drop since the path from inlet to foam is shorter. The seven parallel serpentine channels of the conventional flow-field give a 7 mm^2 inlet cross-sectional area without accounting for the presence of the gas diffusion layer.

Comparing the flow distribution and pressure drop of the different manifold designs, Manifold E is seen to provide the best distribution of flow across the foam and the second lowest pressure drop.

3.2. Hybrid foam flow-field

3.2.1. X-ray computed tomography

The reconstructed X-ray computed tomography scan of the metallic foam with a single pressed flow channel is shown in Fig. 5(a); Fig. 5(b) shows an SEM image of the flow channel. Plastic deformation from the compression of the foam in the flow channel area can be seen in both images. The similarity between the SEM and X-ray CT confirms the validity of the X-ray CT segmentation.

Fig. 5(c) and (d) show the reconstructed cross-section in the x-y plane and the corresponding porosity distribution respectively. Porosity in the area under the flow channel drops from 84% to 15% due to plastic deformation when pressing the flow channel. Minimal porosity reduction is seen on the upper walls of the flow channel, allowing a highly porous route for fluid to move from the flow channels across the bulk of the foam. The minimum thickness of the foam at the centre of the flow channel is 0.3 mm, with 81.3% compression.

3.2.2. Flow distribution

Flow-field area coverage profiles of the metal foam with and without 'hybrid' flow channels are compared in Fig. 6(a). Results show that the presence of flow channels in the foam increases the residence time. This occurs since the flow channels provide a preferential path of low resistance for fluid from inlet to outlet, potentially bypassing areas of foam. Manifold design B with foam pattern B (Fig. 1(g)) exhibits the longest residence time – 4.4 s to reach 80% coverage, 43% longer than without the flow channels. The increased time is due to the flow channels diverting flow away from the top right and bottom left corners of the flow-field. Modifying the manifold and adding another flow channel as in the Manifold E foam pattern C case (Fig. 1(h)) is seen to reduce this effect.

Fig. 7(a) maps the time for different regions of the flow-field to reach 50% concentration for Manifold E and foam pattern C. The pressed flow channels reduce the time taken for the fluid to reach the centre and exit regions of the flow-field. In practice, this would result in reduced reactant concentration gradients and increased temperature uniformity between the opposite ends of the flow-fields. Areas adjacent to the flow channels, particularly in the flow direction, are seen to reach the concentration threshold quickly. This implies that diffusion from the channel into the bulk foam has a lower resistance path to exit than remaining in the channel.

The difference in time to reach 50% concentration with and without the pressed flow channels is shown in Fig. 7(b); a positive time corresponding to a faster coverage with the pressed flow channels present. Reduced times can be seen for the bulk of the flow-field, but especially for the top right corner. In contrast, increased times are on the far left of the flow-field where flow is reduced as it is diverted up the flow channels.

3.2.3. Pressure drop

The pressure drop of different foam flow-fields with and without channels is shown in Fig. 6(b). For Manifold A, the addition of foam pattern A provides a 55% reduction in pressure drop. This is due to an increase in the area over which the fluid can enter the foam. The addition of foam pattern C to Manifold E only generates a 10% reduction in pressure drop since inlet and exit areas are already maximised.

The influence of a single foam channel feature on pressure drop is shown in Fig. 8 for a 55 × 15 × 1.6 mm foam section. Pressing a single channel in the flow direction results in a 2.4 times pressure drop reduction compared to the case without a flow channel, since the channel represents a direct path from inlet to outlet. Pressing a single channel perpendicular to the flow direction produces a 4.0% reduction in pressure drop compared to the no-flow channel case, similar behaviour is seen when two further perpendicular flow channels are added. The pressure drop reduction from the perpendicular channels occurs because the walls of the flow channels maintain the high porosity of the foam when the channel is pressed. This can be seen in the X-ray CT of Fig. 5(b) and flow distribution of Fig. 7. The pressing of channels into the foam can, therefore, provide significant pressure drops in the flow direction, without decreasing permeability in the cross-flow direction.

4. Conclusions

The flow distribution behaviour of porous metallic foam flow-fields has been quantified through ex-situ optical tests using dyed water at Reynolds numbers matched to air. Results demonstrate that the foam distributes fluid efficiently over the flow-field, closely matching the theoretical filling rate until 70% flow-field coverage. After this point, the manifold design influences flow distribution to the corners of the flow-field, with best performance achieved using inlet and exit areas across the width of the flow-field; such as Manifold B and E. Wider foam inlet and exit areas were also seen to reduce the pressure drop to levels lower than a comparable multi-serpentine flow.

The introduction of flow channels into the foam is seen to control
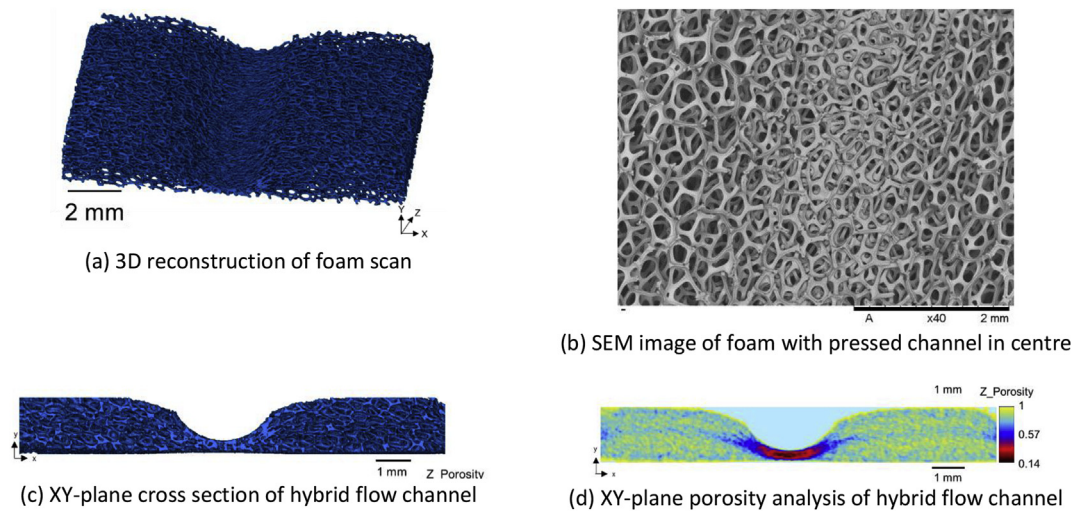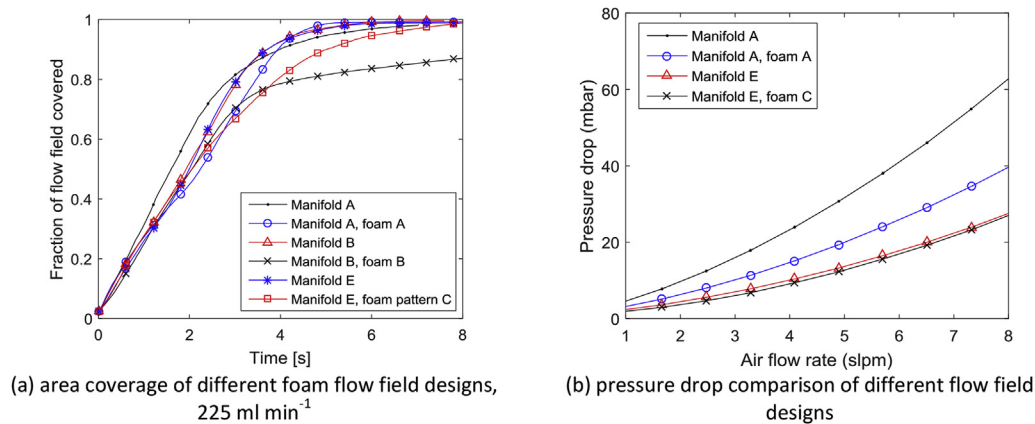
(a) 3D reconstruction of foam scan

(b) SEM image of foam with pressed channel in centre

(c) XY-plane cross section of hybrid flow channel

(d) XY-plane porosity analysis of hybrid flow channel

Fig. 5. 3D reconstruction and SEM images of foam.

(a) area coverage of different foam flow field designs, 225 ml min^{-1}

(b) pressure drop comparison of different flow field designs

Fig. 6. Influence of hybrid foam flow field on area covered profile, high flow.

(a) Time to 50% concentration (s), manifold E foam pattern C

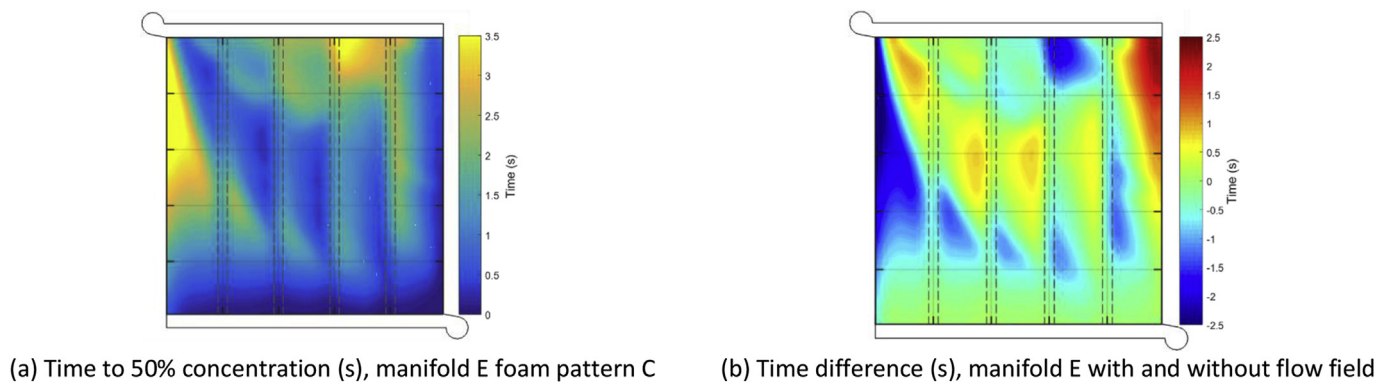(b) Time difference (s), manifold E with and without flow field

Fig. 7. Comparison of time to reach 50% concentration with and without foam flow-fields (grey dashed lines).

flow distribution, whilst simultaneously reducing pressure drop parallel and perpendicular to the flow direction. Further improvements in flow distribution and parasitic loss reductions can be obtained through optimisation of flow channel placement. The influence of flow channels on two-phase flow is also of interest for fuel cell applications.

The findings of this work help to inform future optimised designs of fuel cells utilising porous flow-fields. Reduced residence times and lower parasitic loads have been achieved and improved understanding of how manifold designs influence macroscopic flow distribution developed. A novel 'hybrid' foam and channel flow-field has been introduced for controllable flow distribution.
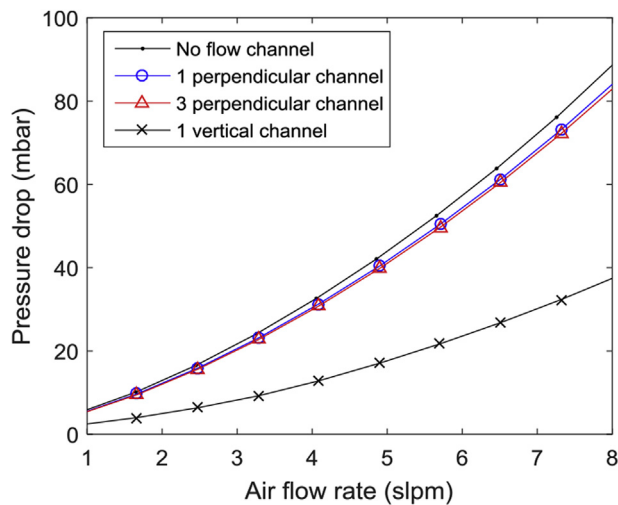
Fig. 8. Influence of flow channel geometry on pressure drop.

References

[1] M.F. Ashby, A. Evans, N.A. Fleck, L.J. Gibson, J.W. Hutchinson, H.N.G. Wadley, Metal Foams : a Design Guide, Butterworth-Heinemann, 2000.

[2] L.-P. Lefebvre, J. Banhart, D.C. Dunand, Porous metals and metallic foams: current status and recent developments, Adv. Eng. Mater. 10 (9) (Sep. 2008) 775–787.

[3] K. Boomsma, D. Poulikakos, F. Zwick, Metal foams as compact high performance heat exchangers, Mech. Mater. 35 (12) (2003) 1161–1176.

[4] H. Huisseune, S. De Schampheleire, B. Ameel, M. De Paepe, Comparison of metal foam heat exchangers to a finned heat exchanger for low Reynolds number applications, Int. J. Heat Mass Tran. 89 (2015) 1–9.

[5] S.T.W. Kuruneru, E. Sauret, S.C. Saha, Y. Gu, Numerical investigation of the temporal evolution of particulate fouling in metal foams for air-cooled heat exchangers, Appl. Energy 184 (Dec. 2016) 531–547.

[6] A. Kouidri, B. Madani, Experimental hydrodynamic study of flow through metallic foams: flow regime transitions and surface roughness influence, Mech. Mater. 99 (2016) 79–87.

[7] P. Zhang, Z.N. Meng, H. Zhu, Y.L. Wang, S.P. Peng, Melting heat transfer characteristics of a composite phase change material fabricated by paraffin and metal foam, Appl. Energy 185 (Jan. 2017) 1971–1983.

[8] M. Odabaee, S. Mancin, K. Hooman, Metal foam heat exchangers for thermal management of fuel cell systems – an experimental study, Exp. Therm. Fluid Sci. 51 (Nov. 2013) 214–219.

[9] E. Afshari, M. Ziaei-Rad, Z. Shariati, A study on using metal foam as coolant fluid distributor in the polymer electrolyte membrane fuel cell, Int. J. Hydrogen Energy 41 (3) (2016) 1902–1912.

[10] W. Yuan, Y. Tang, X. Yang, Z. Wan, Porous metal materials for polymer electrolyte membrane fuel cells – a review, Appl. Energy 94 (Jun. 2012) 309–329.

[11] M. Sajid Hossain, B. Shabani, Metal foams application to enhance cooling of open cathode polymer electrolyte membrane fuel cells, J. Power Sources 295 (2015) 275–291.

[12] O.J. Murphy, A. Cisar, E. Clarke, Low-cost light weight high power density PEM fuel cell stack, Electrochim. Acta 43 (24) (1998) 3829–3840.

[13] A. Kumar, R.G. Reddy, Polymer electrolyte membrane fuel cell with metal foam in the gas flow-field of bipolar/end plates, J. New Mater. Electrochem. Syst. 6 (2003)

231–236.

[14] A. Kumar, R.G. Reddy, Materials and design development for bipolar/end plates in fuel cells, J. Power Sources 129 (1) (2004) 62–67.

[15] A. Kumar, R. Reddy, Modeling of polymer electrolyte membrane fuel cell with metal foam in the flow-field of the bipolar/end plates, J. Power Sources 114 (1) (Feb. 2003) 54–62.

[16] C.-J. Tseng, B.T. Tsai, Z.-S. Liu, T.-C. Cheng, W.-C. Chang, S.-K. Lo, A PEM fuel cell with metal foam as flow distributor, Energy Convers. Manag. 62 (2012) 14–21.

[17] Y.-H. Lee, S.-M. Li, C.-J. Tseng, C.-Y. Su, S.-C. Lin, J.-W. Jhuang, Graphene as corrosion protection for metal foam flow distributor in proton exchange membrane fuel cells, Int. J. Hydrogen Energy 42 (34) (Apr. 2017) 22201–22207.

[18] S. Huo, N.J. Cooper, T.L. Smith, J.W. Park, K. Jiao, Experimental investigation on PEM fuel cell cold start behavior containing porous metal foam as cathode flow distributor, Appl. Energy 203 (Oct. 2017) 101–114.

[19] S. Arisetty, A.K. Prasad, S.G. Advani, Metal foams as flow field and gas diffusion layer in direct methanol fuel cells, J. Power Sources 165 (1) (2007) 49–57.

[20] T. Shudo, K. Suzuki, Performance improvement in direct methanol fuel cells using a highly porous corrosion-resisting stainless steel flow field, Int. J. Hydrogen Energy 33 (11) (Jun. 2008) 2850–2856.

[21] F. Bidault, D.J.L. Brett, P.H. Middleton, N. Abson, N.P. Brandon, A new application for nickel foam in alkaline fuel cells, Int. J. Hydrogen Energy 34 (16) (2009) 6799–6808.

[22] C.-J. Tseng, Y.-J. Heush, C.-J. Chiang, Y.-H. Lee, K.-R. Lee, Application of metal foams to high temperature PEM fuel cells, Int. J. Hydrogen Energy 41 (36) (2016) 16196–16204.

[23] B.-T. Tsai, C.-J. Tseng, Z.-S. Liu, C.-H. Wang, C.-I. Lee, C.-C. Yang, S.-K. Lo, Effects of flow field design on the performance of a PEM fuel cell with metal foam as the flow distributor, Int. J. Hydrogen Energy 37 (17) (2012) 13060–13066.

[24] T. Kariya, T. Hirono, H. Funakubo, T. Shudo, Effects of the porous structures in the porous flow field type separators on fuel cell performances, Int. J. Hydrogen Energy 39 (27) (Sep. 2014) 15072–15080.

[25] Y. Tabe, T. Nasu, S. Morioka, T. Chikahisa, Performance characteristics and internal phenomena of polymer electrolyte membrane fuel cell with porous flow field, J. Power Sources 238 (2013) 21–28.

[26] Q. Meyer, N. Mansor, F. Iacoviello, P.L. Cullen, R. Jervis, D. Finegan, C. Tan, J. Bailey, P.R. Shearing, D.J.L. Brett, Investigation of hot pressed polymer electrolyte fuel cell assemblies via X-ray computed tomography, Electrochim. Acta 242 (2017) 125–136.

[27] Q. Meyer, S. Ashton, P. Boillat, M. Cochet, E. Engebretsen, D.P. Finegan, X. Lu, J.J. Bailey, N. Mansor, R. Abdulaziz, O.O. Taiwo, R. Jervis, S. Torija, P. Benson, S. Foster, P. Adcock, P.R. Shearing, D.J.L. Brett, Effect of gas diffusion layer properties on water distribution across air-cooled, open-cathode polymer electrolyte fuel cells: a combined ex-situ X-ray tomography and in-operando neutron imaging study, Electrochim. Acta 211 (Sep. 2016) 478–487.

[28] F. Jinuntuya, M. Whiteley, R. Chen, A. Fly, The effects of gas diffusion layers structure on water transportation using X-ray computed tomography based Lattice Boltzmann method, J. Power Sources 378 (28) (2018) 53–65.

[29] P. Rama, Y. Liu, R. Chen, H. Ostadi, K. Jiang, Y. Gao, X. Zhang, R. Fisher, M. Jeschke, Simulation of liquid water breakthrough in a nanotomography reconstruction of a carbon paper gas-diffusion layer, Am. Inst. Chem. Eng. J. 58 (2) (2012) 646–655.

[30] R.L. Street, G.Z. Watters, J.K. Vennard, Elementary Fluid Mechanics, J. Wiley, 1996.

[31] D.R. Lide, CRC Handbook of Chemistry and Physics, 96th Edition, (2015).

[32] L. Cheng, A. Spencer, Residence time measurement of an isothermal combustor flow field, Exp. Fluid 52 (3) (2012) 647–661.

[33] Z. Hamadache, A. Spencer, Fuel gallery residence time & heat transfer experimental technique development for gas turbine fuel injectors, 17th Int. Symp. Appl. Laser Tech. to Fluid Mech. vol. 1, 2014, pp. 7–10.

[34] J. Larminie, A. Dicks, Fuel Cell Systems Explained, second ed., J. Wiley, 2003.

[35] A.J. Onstad, C.J. Elkins, F. Medina, R.B. Wicker, J.K. Eaton, Full-field measurements of flow through a scaled metal foam replica, Exp. Fluid 50 (6) (2011) 1571–1585.